**THE EUROPEAN
PHYSICAL JOURNAL C**

Study of the jet shape at 920 GeV/c in proton–nucleus interactions with HERA-B detector

D. Golubkov[1,a], Y. Golubkov[2,b]

[1] Moscow Physical Engineering Institute, 115409 Moscow, Russia
[2] Institute of Nuclear Physics of Moscow State University, 119899 Moscow, Russia

Abstract. We performed a measurement of differential and integral jet shapes in proton-carbon, proton-tungsten and proton-aluminium collisions at 920 GeV/c proton momentum with the HERA-B detector at HERA for the jet transverse energies in the range $4\,\mathrm{GeV} < E_\mathrm{T}(\mathrm{jet}) < 12\,\mathrm{GeV}$. Jets were identified using the k_T-clustering algorithm. The measurements were performed for the hardest jet in the event, directed towards the opposite side with respect to the trigger direction. Jets become narrower with increasing transverse energy and measured distributions agree well with predictions of the PYTHIA 6.2 model. We do not observe any significant difference in the jet shape for the carbon and the aluminium targets. Nevertheless, the transverse energy flow at small and large radii for the tungsten sample is slightly less than for light nuclei. This observation indicates some influence of the nuclear environment on the formation of jets in heavy nuclei, especially at lower transverse energies, $5\,\mathrm{GeV} < E_\mathrm{T}(\mathrm{jet}) < 6\,\mathrm{GeV}$.

PACS. 13.85.-t; 13.87.-a; 13.87.Fh

1 Introduction

The parton $\to$ hadron transition is one of the most interesting outstanding questions in QCD and we should look inside jets to better understand this process.

In the standard model our general understanding of high-energy collisions of hadrons suggests that jets arise when short-distance, large-momentum-transfer interactions generate partons (quarks and gluons) that are widely separated in momentum space just after the hard collision. In a fashion that is not yet quantitatively understood in detail these configurations are thought to evolve into hadronic final states exhibiting collimated sprays of hadrons, which are called jets. Thus jets can be regarded as a universal signal of parton dynamics at short distances.

Hadron collisions are a perfect place to perform such studies, because they are a high rate source of jets over a very wide range of QCD scales in the same experiment. High-p_T jets dominate the event structure in hadronic collisions at high center-of-mass (CM) energies $\sqrt{s}$ when sufficiently large transverse energy E_T is required. This was demonstrated by various experiments at $\sqrt{s} = 63\,\mathrm{GeV}$ [1], at $\sqrt{s} = 540\,\mathrm{GeV}$ [2, 3], at $\sqrt{s} = 1800\,\mathrm{GeV}$ [4, 5] at hadronic colliders.

At large transverse energies ($E_\mathrm{T} \sim 100\,\mathrm{GeV}$) the corrections to jet shape from parton fragmentation are usually

[a] e-mail: dimgol@mail.desy.de
[b] e-mail: golubkov@mail.desy.de

considered to be small in comparison to ones due to the parton cascade initiated by the high-E_T scattered parton. But at the more moderate transverse energies $\sim$ of a few GeV, this conclusion is not valid. Thus the investigation of the jet structure at moderate energies in hadronic collisions can give important information about parton fragmentation processes in hadronic interactions.

Measurements of jets in fixed-target experiments not only widen the energy range of jet studies but, in addition, enable extension of these studies into a new realm of colliding particles: meson-nucleon and hadron-nucleus interactions.

At lower $\sqrt{s}$, because of contributions from mechanisms such as initial- and final-state parton radiation and multiple scattering of quarks and gluons, the event structure rarely exhibits dijet topology and the jet signal is rather difficult to extract experimentally [6, 7]. Nevertheless, the presence of jet structure has also been demonstrated in fixed target experiments at lower energies specifically at 800 GeV in pA-collisions [8], and at 500 GeV in both pBe and πBe-collisions [9]. Also a jet signal consistent with QCD predictions and with extrapolations of jet cross sections from higher CM energies was found by [10, 11].

The methods employed to extract jets at moderate CM energies depend heavily on Monte Carlo models. Therefore, the absolute cross sections for jet production determined at these energies are subject to large systematic errors. However, the relative dependence of jet production and properties from different nuclear tar-

gets should be less sensitive to the assumed jet size and background.

There is a large variety of jet-shape variables, they are very informative and enter all hard processes with features which are expected to be universal (QCD factorization). In the present analysis we concentrate on studies of the internal jet structure, measuring the differential and integral jet shape.

2 Jet definition

A jet is qualitatively defined as a collimated spray of high-energy hadrons. However, for the purpose of performing accurate quantitative studies, one needs a precise definition of a jet. Essentially, one has to specify how low-energy particles are assigned to jets, in order to have infrared-finite cross sections.

The standard "Snowmass convention" on jet 3-momentum definition [12] is:

$$
\begin{aligned}
E_{\mathrm{T}}(\mathrm{jet}) &= \sum_i p_{\mathrm{T},i}\,, \\
\eta(\mathrm{jet}) &= \sum_i p_{\mathrm{T},i}\eta_i/E_{\mathrm{T}}(\mathrm{jet})\,, \\
\phi(\mathrm{jet}) &= \sum_i p_{\mathrm{T},i}\phi_i/E_{\mathrm{T}}(\mathrm{jet})\,,
\end{aligned}
\tag{1}
$$

with $E_{\mathrm{T}}(\mathrm{jet}), \eta(\mathrm{jet}), \phi(\mathrm{jet})$ being the jet transverse energy, pseudo-rapidity and azimuthal angle, respectively, and $p_{\mathrm{T},i}, \eta_i, \phi_i$ are transverse energy, pseudo-rapidity and azimuthal angle of particles, forming the jet. Usage of the above observables ensures the invariance of the jet momentum definition with respect to longitudinal Lorentz boosts.

Beside the above general definition of the jet's characteristics one needs to specify an algorithm – how to assign a particle to one of the jets in the event. The most usable at present are two algorithms – "cone" and "k_{T}" (or "Durham") algorithms.

The simplest cone algorithm (see, e.g., [12]) starts from a "jet initiator" – a particle with transverse momentum above a predefined threshold, e.g., $p_{\mathrm{T}} \geq 1$ GeV, adjoining to the initiator particles within a cone of radius $r \leq R_{\mathrm{c}}$. Here $r = \sqrt{\Delta\eta^2 + \Delta\phi^2}$ and $R_{\mathrm{c}} \approx 0.7$. There are modifications of this algorithm, using an iterative procedure to define the current jet axis. The cone algorithm is suitable for e^+e^- collisions, where the remnants of the initial particles are absent. For hadronic interactions and deep-inelastic lepton-hadron scattering, the cone algorithm meets problems with particles separation in multi-jet events as well problems when being compared with NLO and NNLO QCD calculations.

On the other hand the k_{T} algorithm [13,14] is expected to be the best for hadronic collisions because it is based on the QCD picture of jet development. This algorithm is invariant under longitudinal Lorentz boosts and is infrared and collinear safe. It has been shown [15] that the inclusive k_{T} cluster algorithm provides, at present, the best jet finding algorithm from the theoretical point of view, since the

problem of overlapping jets, which affects, e.g., the iterative cone algorithm [16], is avoided.

The measure of the "closeness" of two particles/protojets in the k_{T} algorithm is:

$$
d_{ij} = \min\left(p_{\mathrm{T},i}^2, p_{\mathrm{T},j}^2\right)\left[(\eta_i - \eta_j)^2 + (\phi_i - \phi_j)^2\right]\,.
\tag{2}
$$

We use here the original expression for d_{ij} [13] without the additional parameter R_0 suggested in [17], where the measure (2) is replaced by d_{ij}/R_0^2. Because the parameter R_0 is to be around unity, it does not make sense to introduce R_0 in our case. At small angles between two particles the measure, d_{ij}, is, approximately, the squared relative transverse momentum of one of the particles with respect to the other particle.

The k_{T} algorithm looks as following [13]:

1. For each protojet, define $d_i = E_{\mathrm{T},i}^2$ and for each pair of protojets define d_{ij} from (2)
2. Find the smallest of all the d_i and d_{ij} and label it $d_{\min}$
3. If $d_{\min}$ is a d_{ij}, merge protojets i and j into a new protojet k according to (1)
4. If $d_{\min}$ is a d_i, the corresponding protojet i is "not mergeable". Remove it from the list of protojets and add it to the list of jets.

Repeating the above four steps till there are "mergeable" protojets one subdivides the event into a number of groups of particles where each particle is assigned to one and only one group/jet.

3 Jet shape observables

In the present work we measure the differential $\rho(r)$ and integral $\Psi(r)$ jet shapes characterizing how widely a jet's energy is spread in the (η, ϕ) plane. Jet shape is one of the most popular characteristics of jet structure in hadron collisions. Jet shape $\Psi(r)$ is defined as the transverse energy flow within the cone of radius r around the jet axis in (η, ϕ) plane normalized to unity and averaged over all jets in the (sub)sample. The differential jet shape $\rho(r)\,dr$ is the derivative of $\Psi(r)$ over r and is the transverse energy flow through the annulus of width dr with radius r around the jet axis.

These observables are, in general, collinear safe (for two particles with parallel momenta $\mathbf{p}_i, \mathbf{p}_j$ one may replace these two particles with a single one with a momentum equal to $\mathbf{p}_i + \mathbf{p}_j$) and infra-red safe (for $p_i \ll p_j$ one may neglect p_i) [18]. This implies that one may assume *parton-flow* $\approx$ *hadron-flow*. Particles include both charged particles measured by the tracker detector and clusters in the electromagnetic calorimeter.

More quantitatively, the observables $\Psi(r)$ and $\rho(r)$ are defined as follows:

$$
\begin{aligned}
\Psi(r) &= \int_0^r \mathrm{d}r'\rho(r')\,, \\
\rho(r) &= 2\pi r \int_0^{E_{\mathrm{T}}(\mathrm{jet})} \mathrm{d}p_{\mathrm{T}} \frac{p_{\mathrm{T}}(r)}{E_{\mathrm{T}}(\mathrm{jet})} \frac{\mathrm{d}^2 n(r, p_{\mathrm{T}})}{\mathrm{d}r\,\mathrm{d}p_{\mathrm{T}}}\,,
\end{aligned}
\tag{3}
$$

where r is the distance to the jet axis in (η, ϕ) plane, p_T is the transverse momentum of a particle, and $\frac{\mathrm{d}^2 n(r, p_T)}{\mathrm{d}r\, \mathrm{d}p_T}$ is the particle number density over r and p_T.

In the present work we study also the dependence of jet structure on atomic number of a target nucleus. In principle, there may exist an uncertainty with choice of the center of mass reference frame – either (pp), or (pn) or (pA). To avoid this problem we perform our analysis in the laboratory reference frame.

Due to the above uncertainty with the choice of reference frame we do not present the more traditional longitudinal and transversal (with the respect of the jet axis) distributions of particles ("fragmentation function"). These observables are not invariant under longitudinal Lorentz boosts and usually are given in the beam-target center of mass system.

4 HERA-B detector and data sample

4.1 Detector

HERA-B is a fixed target experiment operated at the 920 GeV proton storage ring of HERA at DESY [19].

A plan view of the HERA-B spectrometer is shown in Fig. 1. The spectrometer dipole magnet provides a field integral of 2.13 T-m, with the main component perpendicular to the x–z plane. The apparatus (including particle identification counters) has a forward acceptance of 15–220 mrad in the bending plane and 15–160 mrad in the non-bending plane. The experiment uses a multi-wire fixed target which operates in the halo of the proton beam during HERA e-p collider operation. Up to eight different targets can be operated simultaneously, with their positions being adjusted dynamically in order to maintain a constant interaction rate between 1 and 40 MHz.

The tracking system consists of a vertex detector system (VDS) [21] and a main tracker system. The VDS features 64 double-sided silicon microstrip detectors arranged in eight stations along, and four quadrants around, the proton beam. The silicon strips have a readout pitch of approximately 50 μm. Particle identification was performed by a ring imaging Cherenkov detector (RICH) [25], an electromagnetic calorimeter (ECAL) [26] and a muon detector (MUON) [27].

The main tracking system is separated into an inner tracker (ITR) [22] close to the proton beam-pipe and an outer tracker (OTR) [23, 24] farther out. The tracker system covers pseudorapidities within a range of approximately $2 \leq \eta \leq 4.8$ in the laboratory system. Magnetic analysis for the OTR ensures the relative momentum resolution around $\Delta p/p \approx 5 \times 10^{-5} p \oplus 1.6 \times 10^{-2}$.

The electromagnetic calorimeter ECAL is based on "shashlyk" sampling calorimeter technology, consisting of scintillator layers sandwiched between metal absorbers. In the radially innermost section tungsten was used as an absorber, and lead everywhere else. ECAL covers pseudorapidities within a range of approximately $2 \leq \eta \leq 5.2$ in laboratory system. Calorimeter towers have a depth of about 20 radiation lengths with granularity approximately 2.2×2.2 cm, 5.58×5.58 cm, and 11.15×11.15 cm for inner, middle and outer sections respectively. Energy resolution $\Delta E/E$ is $20.5\%/\sqrt{E} \oplus 1.2\%$ for inner section and approximately $11\%/\sqrt{E} \oplus 1.0\%$ for middle and outer sections.

4.2 Data sample

For the analysis presented here, only data from VDS, OTR and the ECAL were used with carbon (C), aluminium (Al),
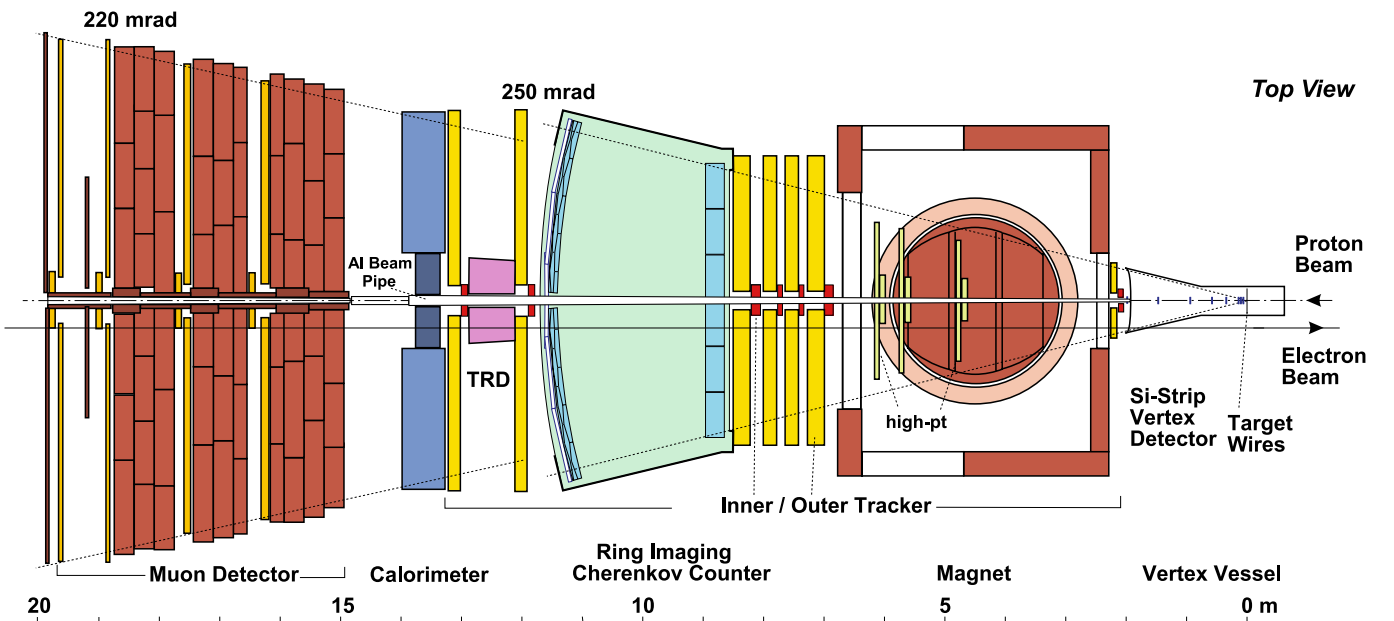

Fig. 1. Schematic top view of the HERA-B detector

and tungsten (W) wire targets. The inner tracker was not used due to its insufficient stability.

We used data collected in so called "high E_T" runs, i.e., runs in which about half of the events in each run were required to satisfy a calorimeter pre-trigger. The "high E_T" pre-trigger demands a transverse energy deposition at least in one of the ECAL towers above a predefined threshold, $E_T \geq E_T(min)$. The remaining events in these runs were collected with a random interaction trigger, in fact, minimum bias events. The data were recorded at a moderate interaction rate, 1–3 MHz, which corresponds to ≈ 0.1–0.3 interactions per filled bunch crossing. Therefore only a small fraction of events contain more than one interaction. Tungsten data were collected with pre-scaling by a factor 2.

The results presented here are based on a sample of ≈ 18 million events collected in the period from December 2002 to March 2003. There were three runs with a carbon target, two runs with a tungsten target, and three runs with an aluminium target with ECAL pre-trigger either $E_T > 3$ GeV or $E_T > 2$ GeV. Note that about 40% of triggers were produced by ECAL clusters matched with tracks/segments in tracking detector.

For the additional off-line event selection, we require that the ECAL cluster with maximal transverse momentum (called in the following the "trigger cluster") has $p_T^{max} \geq 3.0$ GeV. The choice of the cluster with maximal p_T unifies the selection of data and MC samples. This "trigger cluster" does not necessarily coincide with the ECAL cluster which produced the hardware pre-trigger. But the pre-trigger and the hardest ECAL clusters differ in less than 0.1% of events.

Events were required to have a reconstructed primary vertex. The track and cluster selection criteria are the following:

– Track must start in the VDS,
– Track must be successfully fitted over the whole length (OTR and VDS),
– "Clones" (nearby reconstructed tracks originating from the same real physical track) are removed,
– EM clusters must not match any track or track segment in the OTR,
– The trigger conditions are tested before the check on track-cluster matching. If the trigger cluster matches a track or a track segment, the event is accepted, but the trigger cluster itself is removed from further analysis.

After applying above selection criteria we have for our analysis approximately 1 097 000 carbon events, 447 000 tungsten events and 1 002 000 aluminium events.

We considered only the jet with the maximal transverse energy in the event. Because our trigger is based on measuring the electromagnetic clusters in the ECAL, it can distort properties of the selected jets, preferring the jets enriched by gammas/π^0's. To avoid this problem, we accepted only "away-side" jets, i.e., jets directed in the opposite direction with respect to the trigger cluster in the plane perpendicular to the beam axis, demanding $|\phi(\text{jet}) - \phi(\text{trig})| \geq 90°$. The Monte Carlo simulation shows that

such a selection gives minimal distortion of the jet transverse energy and its direction in comparison to the parent parton.

To minimize effects of the restricted acceptance we accept jets with axes in the narrow pseudo-rapidity range $3.4 \leq \eta(\text{jet}) \leq 3.6$.

5 Monte Carlo simulation

The simulation of the physical processes and the detector response in modern experiments is one of the crucial parts of data analysis. For the simulation of jet events in HERA-B, the main problem is that existing generators describing the hadron(nucleus)-nucleus collisions, are intended for the study of minimum bias physics and soft processes. Therefore their use for simulation of hard hadron-nucleus collisions is extremely inefficient (if it is possible at all). Due to these problems a procedure for the description of hard parton scattering, taking into account soft interactions in the nucleus was developed.

The bases of the developed MC generator are theoretical expectations as well as experimental evidence [8, 9] that at moderate energies $\sqrt{s} \approx 40$ GeV, the hard-scattering mechanism already dominates pp collisions, whereas soft scattering is still the dominant mechanism for the proton collisions with heavy nuclei. This interpretation is consistent with the decrease of nuclear effects with increasing jet E_T. All available data on the hadroproduction of jets are consistent with a rather modest nuclear enhancement (the parameter α in A-dependence is close to unity, $\alpha < 1.10$), diminishing with increasing jet E_T.

This fact allows us to discriminate hard and soft processes and to exploit the existing MC models for hard parton scattering to simulate jet production in proton-nucleus collisions.

We use PYTHIA 6.2 [28] to produce hadronic systems in parton-parton scattering, adding to the hard system soft particles produced in the collision of the proton remnant with the nucleus. Note that in PYTHIA, the partonic processes are simulated using LO matrix elements with the inclusion of initial- and final-state parton showers.

The program FRITIOF 7.02 [29] from CERN library (including ARIADNE 4.02 as a part of FRITIOF package) has been adapted to double precision to make it compatible with PYTHIA 6.2. Because the FRITIOF package is heavily based on PYTHIA, all parameters for soft (semi-hard) processes in FRITIOF are the default parameters of PYTHIA 6.2 in the adapted version of FRITIOF.

In such a combined PYTHIA 6.2/FRITIOF 7.02 package the event simulation procedure consists of the following steps:

– Simulation of the hard sub-process(es) (parton-parton scattering) with PYTHIA in pN collision (a nucleon N is being chosen randomly according to the nucleus content),
– The independent fragmentation of scattered partons is performed,
– Resulting stable particles (hard system) are saved,

– Simulation of the soft collision is performed by the FRI-TIOF generator as a pA interaction with energy remaining after the hard scattering,[1]
– The transverse momenta of the whole system are balanced, preserving the 4-momentum of the hard system,
– The final fragmentation and decays are performed.

The main PYTHIA inputs used for hard scattering are the following:

– Proton structure function "CTEQ2L (best LO fit)" from PDFLIB,
– Intrinsic $k_T = 1 \, \text{GeV}$ of partons (default for PYTHIA 6.2),
– Independent fragmentation of final state partons from the hard process,
– String fragmentation in soft interactions with the nucleus (in FRITIOF),
– Lund symmetric fragmentation model both for independent and string fragmentation,
– QCD scale for parton-parton scattering as is the default for PYTHIA 6.2.

We tested that the default set of PYTHIA inputs gives a quite satisfactory description of our data as well as a good reproduction of the prompt photon p_T distribution measured by experiment E-706 [30, 31] in pBe collisions at $\sqrt{s} = 38.8 \, \text{GeV}$.

Note here that because we restricted our studies to the narrow range $\Delta\eta = \pm 0.1$ the variation of the PDF does not play any rôle. We also checked that the choice of the QCD scale for parton scattering is not significant in our range of transverse momenta and pseudo-rapidities.

The main effect comes from the intrinsic transverse momentum, k_T, of partons. In paper [30, 31] the authors suggest the value $k_T = 1.3 \, \text{GeV}$ to describe their results on prompt photon production. But we did not find a significant difference between the values $k_T = 1.3 \, \text{GeV}$ and the default PYTHIA 6.2 value, $k_T = 1.0 \, \text{GeV}$ for our conditions and use the default PYTHIA 6.2 value.

To increase the simulation efficiency the parton subprocesses were simulated with the cut $p_T(\text{hard}) \geq 3 \, \text{GeV}$, where the $p_T(\text{hard})$ is the transverse momentum of the outgoing γ/parton. Such a cut increases the simulation efficiency by a few orders of magnitude in comparison to the default cut in PYTHIA for hard scattering $p_T(hard) \geq 1 \, \text{GeV}$.

The simulation of the detector response was carried out using the GEANT 3.21 package with subsequent standard HERA-B reconstruction of the simulated events. We applied the same selection criteria for tracks and EM clusters as for real data. In the MC sample we also removed from consideration (as in data) the so called "hot modules" in ECAL. "Hot modules" cover a negligibly small fraction of the total ECAL acceptance and, in fact, do not affect the presented results. In total, after selection (without trigger cut), the number of MC events is approximately equal to experimental statistics – 1 499 000 events for the

carbon target, 571 400 events for the tungsten target and 1 016 600 events for the aluminium target.

6 Results

The measured, raw differential jet shape distribution $\rho(r)$ was created by storing the entries in the bin Δr with weight $p_T/E_T(\text{jet})$ and further dividing this distribution by the bin width Δr.

To correct the measured jet shape distributions for acceptance and reconstruction distortions (systematic corrections) we used bin-by-bin corrections. Corrections for $\rho(r)$ were calculated in each bin of jet transverse energy E_T separately and can be written as:

$$\rho(r; E_T) = R(r; E_T) \times \rho_m(r; E_T)$$
$$R(r; E_T) = \rho_g(r; E_T)/\rho_r(r; E_T) \tag{4}$$

where, ρ and ρ_m are corrected and measured distributions and ρ_r and ρ_g are simulated distributions at the reconstructed and generator levels, respectively.

We tested the quality of the track information to check for possible systematic biases in the track momentum measurements. For this purpose we reconstructed known resonances K^0, ρ^0, K^{*0}, ϕ^0, and Λ^0. Results for reconstructed masses are in good agreement with the known values of the particle data group [32]. Thus we don't expect any significant systematic bias in measured track momenta.

We checked, that after applying the trigger cut $p_T^{\max} > 3 \, \text{GeV}$, the simulated distributions for jets and particles agree well with data except for the multiplicity distributions for low-p_T particles, where simulated events have lower average multiplicity. This discrepancy is a known problem of the FRITIOF generator. But this discrepancy does not distort jet shape distribution in the selected jets and does not play a significant rôle in bin-by-bin correction procedure.

The trigger cut, $p_T^{\max} > 3 \, \text{GeV}$, leaves about 0.5% of the total MC sample. Using the simulated sample, we checked that the event triggering does not distort the jet shape for "away-side" jets. We checked also that triggered and non-triggered MC samples both give good description of the data jet shape within respective statistical errors. This fact allows us to use the non-triggered MC sample to find systematic corrections $R(r; E_T)$, thus reducing statistical systematic errors by more than an order of magnitude.

We performed measurements of the jet shape in the range of jet transverse energies $E_T > 5 \, \text{GeV}$, to minimize the influence of the cut $p_T(hard) > 3 \, \text{GeV}$ which we applied when simulating parton-parton scattering. Due to the presence of the Gaussian-distributed intrinsic transverse momentum with width $k_T = 1 \, \text{GeV}$, the missing range of parton transverse momenta, $p_T < 3 \, \text{GeV}$, gives a negligible contribution to the jet yield for $E_T > 5 \, \text{GeV}$. In this case one can expect that MC based systematic corrections give reliable results.

---

[1] We also tested the simulation of πA collisions for the remnant. The difference is insignificant.

We could select jets up to transverse energy $E_T \leq$ 14 GeV, however, for $E_T > 10$ GeV, the statistics is small due to the steeply falling jet E_T spectrum. Therefore, we divide E_T(jet) range 5–10 GeV into five equal bins and chose one bin for $E_T > 10$ GeV. We apply bin-by-bin corrections (4) to measured differential jet shape $\rho(r)$ in each E_T(jet) bin.

Our results for differential and integral jet shapes are presented in Tables 1 and 2 for the carbon target, in Ta-bles 3 and 4 for the aluminium target and in Tables 5 and 6 for the tungsten target. We take as a systematic error the uncertainty on the correction factors defined by the finite Monte Carlo statistics. Our studies show that MC uncertainties dominate the other possible sources of systematic errors. Errors given in the tables are the quadratic sum of statistical and systematic errors. Both types of errors are, approximately, equal each to other. The corrected $\Psi(r; E_T)$ distribution was obtained by integration of the

Table 1. Differential and integral jet shapes for carbon for 5 GeV $< E_T < 8$ GeV

r	$E_T = 5$–6 GeV ρ	Ψ	$E_T = 6$–7 GeV ρ	Ψ	$E_T = 7$–8 GeV ρ	Ψ
0.05	0.550 ± 0.040	0.055 ± 0.004	0.550 ± 0.050	0.055 ± 0.005	0.420 ± 0.050	0.042 ± 0.005
0.15	1.250 ± 0.050	0.180 ± 0.006	1.210 ± 0.060	0.176 ± 0.008	1.050 ± 0.080	0.147 ± 0.009
0.25	1.510 ± 0.050	0.331 ± 0.008	1.390 ± 0.060	0.320 ± 0.010	1.500 ± 0.100	0.295 ± 0.014
0.35	1.440 ± 0.040	0.476 ± 0.009	1.410 ± 0.050	0.460 ± 0.010	1.430 ± 0.080	0.438 ± 0.016
0.45	1.370 ± 0.040	0.613 ± 0.009	1.410 ± 0.050	0.600 ± 0.010	1.420 ± 0.070	0.580 ± 0.020
0.55	1.200 ± 0.030	0.730 ± 0.010	1.120 ± 0.040	0.710 ± 0.010	1.120 ± 0.060	0.690 ± 0.020
0.65	0.880 ± 0.020	0.820 ± 0.010	0.890 ± 0.030	0.800 ± 0.010	0.900 ± 0.040	0.780 ± 0.020
0.75	0.630 ± 0.020	0.880 ± 0.010	0.680 ± 0.020	0.866 ± 0.014	0.750 ± 0.040	0.860 ± 0.020
0.85	0.460 ± 0.010	0.930 ± 0.010	0.490 ± 0.020	0.915 ± 0.014	0.470 ± 0.020	0.900 ± 0.020
0.95	0.287 ± 0.009	0.960 ± 0.010	0.358 ± 0.014	0.951 ± 0.014	0.380 ± 0.020	0.940 ± 0.020
1.05	0.177 ± 0.006	0.980 ± 0.010	0.220 ± 0.010	0.973 ± 0.014	0.242 ± 0.015	0.970 ± 0.020
1.15	0.112 ± 0.005	0.990 ± 0.010	0.122 ± 0.006	0.985 ± 0.014	0.150 ± 0.010	0.980 ± 0.020
1.25	0.057 ± 0.003	0.990 ± 0.010	0.076 ± 0.004	0.992 ± 0.014	0.097 ± 0.008	0.990 ± 0.020
1.35	0.032 ± 0.002	1.000 ± 0.010	0.039 ± 0.003	0.996 ± 0.014	0.049 ± 0.005	1.000 ± 0.020
1.45	0.017 ± 0.001		0.019 ± 0.002	0.998 ± 0.014	0.024 ± 0.003	
1.55	0.008 ± 0.001		0.011 ± 0.001	0.999 ± 0.014	0.011 ± 0.002	
1.65	0.003 ± 0.001		0.005 ± 0.001	1.000 ± 0.014	0.006 ± 0.001	
1.75	0.001 ± 0.001		0.001 ± 0.001		0.003 ± 0.001	
1.85			0.001 ± 0.001		0.001 ± 0.001	

Table 2. Differential and integral jet shapes for carbon for $E_T > 8$ GeV

r	$E_T = 8$–9 GeV ρ	Ψ	$E_T = 9$–10 GeV ρ	Ψ	$E_T > 10$ GeV ρ	Ψ
0.05	0.280 ± 0.040	0.028 ± 0.004	0.280 ± 0.050	0.027 ± 0.005	0.150 ± 0.060	0.015 ± 0.006
0.15	0.900 ± 0.100	0.121 ± 0.010	0.700 ± 0.100	0.100 ± 0.010	1.000 ± 0.300	0.120 ± 0.030
0.25	1.350 ± 0.140	0.256 ± 0.020	1.140 ± 0.160	0.220 ± 0.020	1.600 ± 0.300	0.280 ± 0.040
0.35	1.300 ± 0.100	0.383 ± 0.020	1.600 ± 0.200	0.370 ± 0.030	1.400 ± 0.300	0.420 ± 0.050
0.45	1.400 ± 0.100	0.529 ± 0.020	1.600 ± 0.200	0.530 ± 0.040	1.400 ± 0.200	0.560 ± 0.050
0.55	1.220 ± 0.090	0.651 ± 0.030	1.200 ± 0.100	0.650 ± 0.040	1.130 ± 0.150	0.670 ± 0.060
0.65	1.040 ± 0.070	0.755 ± 0.030	0.960 ± 0.090	0.750 ± 0.040	0.670 ± 0.090	0.740 ± 0.060
0.75	0.790 ± 0.060	0.835 ± 0.030	0.650 ± 0.060	0.810 ± 0.040	0.640 ± 0.090	0.800 ± 0.060
0.85	0.550 ± 0.040	0.889 ± 0.030	0.620 ± 0.060	0.880 ± 0.040	0.560 ± 0.080	0.860 ± 0.060
0.95	0.430 ± 0.030	0.933 ± 0.030	0.380 ± 0.040	0.910 ± 0.040	0.470 ± 0.080	0.910 ± 0.060
1.05	0.260 ± 0.020	0.959 ± 0.030	0.340 ± 0.040	0.950 ± 0.040	0.360 ± 0.060	0.940 ± 0.060
1.15	0.200 ± 0.020	0.979 ± 0.030	0.220 ± 0.030	0.970 ± 0.040	0.130 ± 0.030	0.960 ± 0.060
1.25	0.100 ± 0.010	0.989 ± 0.030	0.130 ± 0.020	0.980 ± 0.040	0.190 ± 0.040	0.970 ± 0.060
1.35	0.050 ± 0.007	0.994 ± 0.030	0.084 ± 0.015	0.990 ± 0.040	0.130 ± 0.030	0.990 ± 0.060
1.45	0.023 ± 0.004	0.996 ± 0.030	0.050 ± 0.010	1.000 ± 0.040	0.050 ± 0.020	0.990 ± 0.060
1.55	0.015 ± 0.003	0.998 ± 0.030	0.028 ± 0.009		0.040 ± 0.010	1.000 ± 0.060
1.65	0.015 ± 0.006	0.999 ± 0.030	0.015 ± 0.006		0.040 ± 0.020	
1.75	0.002 ± 0.001	1.000 ± 0.030	0.005 ± 0.002		0.007 ± 0.004	
1.85	0.002 ± 0.002		0.004 ± 0.003		0.008 ± 0.005	
1.95					0.003 ± 0.003	

Table 3. Differential and integral jet shapes for aluminium 5 GeV $< E_{\mathrm{T}} <$ 8 GeV

r	$E_{\mathrm{T}} = 5{-}6$ GeV		$E_{\mathrm{T}} = 6{-}7$ GeV		$E_{\mathrm{T}} = 7{-}8$ GeV	
	ρ	Ψ	ρ	Ψ	ρ	Ψ
0.05	0.660 ± 0.050	0.066 ± 0.005	0.580 ± 0.060	0.058 ± 0.006	0.430 ± 0.050	0.043 ± 0.005
0.15	1.230 ± 0.050	0.189 ± 0.007	1.220 ± 0.070	0.179 ± 0.009	1.160 ± 0.100	0.160 ± 0.010
0.25	1.480 ± 0.050	0.337 ± 0.009	1.510 ± 0.080	0.330 ± 0.010	1.400 ± 0.100	0.303 ± 0.016
0.35	1.450 ± 0.040	0.480 ± 0.010	1.420 ± 0.060	0.470 ± 0.010	1.480 ± 0.090	0.450 ± 0.020
0.45	1.380 ± 0.040	0.620 ± 0.010	1.340 ± 0.050	0.610 ± 0.010	1.250 ± 0.070	0.580 ± 0.020
0.55	1.120 ± 0.030	0.730 ± 0.010	1.150 ± 0.040	0.722 ± 0.015	1.060 ± 0.060	0.680 ± 0.020
0.65	0.870 ± 0.020	0.820 ± 0.010	0.850 ± 0.030	0.806 ± 0.015	0.950 ± 0.050	0.780 ± 0.020
0.75	0.660 ± 0.020	0.880 ± 0.010	0.670 ± 0.020	0.874 ± 0.016	0.750 ± 0.040	0.850 ± 0.020
0.85	0.450 ± 0.014	0.930 ± 0.010	0.480 ± 0.020	0.922 ± 0.016	0.560 ± 0.030	0.910 ± 0.020
0.95	0.290 ± 0.010	0.960 ± 0.010	0.310 ± 0.010	0.953 ± 0.016	0.350 ± 0.020	0.940 ± 0.020
1.05	0.194 ± 0.008	0.980 ± 0.010	0.200 ± 0.010	0.973 ± 0.016	0.247 ± 0.016	0.970 ± 0.020
1.15	0.111 ± 0.005	0.990 ± 0.010	0.123 ± 0.007	0.985 ± 0.016	0.150 ± 0.010	0.980 ± 0.020
1.25	0.063 ± 0.003	0.990 ± 0.010	0.074 ± 0.005	0.993 ± 0.016	0.086 ± 0.007	0.990 ± 0.020
1.35	0.030 ± 0.002	1.000 ± 0.010	0.038 ± 0.003	0.996 ± 0.016	0.042 ± 0.005	1.000 ± 0.020
1.45	0.016 ± 0.001		0.022 ± 0.002	0.999 ± 0.016	0.024 ± 0.003	
1.55	0.008 ± 0.001		0.009 ± 0.001	0.999 ± 0.016	0.009 ± 0.002	
1.65			0.004 ± 0.001	1.000 ± 0.016	0.009 ± 0.002	
1.75			0.001 ± 0.001		0.004 ± 0.001	
1.85					0.002 ± 0.001	
1.95					0.001 ± 0.001	

Table 4. Differential and integral jet shapes for aluminium $E_{\mathrm{T}} >$ 8 GeV

r	$E_{\mathrm{T}} = 8{-}9$ GeV		$E_{\mathrm{T}} = 9{-}10$ GeV		$E_{\mathrm{T}} > 10$ GeV	
	ρ	Ψ	ρ	Ψ	ρ	Ψ
0.05	0.340 ± 0.050	0.034 ± 0.005	0.300 ± 0.060	0.030 ± 0.006	0.170 ± 0.060	0.017 ± 0.006
0.15	1.000 ± 0.100	0.130 ± 0.010	0.600 ± 0.100	0.090 ± 0.010	0.900 ± 0.200	0.110 ± 0.020
0.25	1.440 ± 0.150	0.280 ± 0.020	1.300 ± 0.200	0.220 ± 0.020	1.200 ± 0.200	0.230 ± 0.030
0.35	1.300 ± 0.100	0.400 ± 0.020	1.300 ± 0.200	0.360 ± 0.030	1.600 ± 0.300	0.390 ± 0.040
0.45	1.300 ± 0.100	0.530 ± 0.030	1.300 ± 0.150	0.490 ± 0.030	1.000 ± 0.200	0.490 ± 0.040
0.55	1.300 ± 0.100	0.660 ± 0.030	1.300 ± 0.100	0.610 ± 0.040	1.200 ± 0.200	0.610 ± 0.050
0.65	1.030 ± 0.080	0.760 ± 0.030	1.000 ± 0.100	0.710 ± 0.040	0.900 ± 0.100	0.700 ± 0.050
0.75	0.740 ± 0.050	0.830 ± 0.030	0.900 ± 0.100	0.800 ± 0.040	0.550 ± 0.080	0.750 ± 0.050
0.85	0.500 ± 0.040	0.880 ± 0.030	0.600 ± 0.060	0.860 ± 0.040	0.700 ± 0.200	0.820 ± 0.060
0.95	0.480 ± 0.040	0.930 ± 0.030	0.540 ± 0.060	0.920 ± 0.040	0.600 ± 0.100	0.880 ± 0.060
1.05	0.270 ± 0.020	0.960 ± 0.030	0.330 ± 0.040	0.950 ± 0.040	0.400 ± 0.100	0.920 ± 0.060
1.15	0.152 ± 0.015	0.970 ± 0.030	0.180 ± 0.030	0.970 ± 0.040	0.400 ± 0.100	0.960 ± 0.060
1.25	0.121 ± 0.014	0.990 ± 0.030	0.160 ± 0.030	0.980 ± 0.040	0.180 ± 0.030	0.980 ± 0.060
1.35	0.070 ± 0.010	0.990 ± 0.030	0.082 ± 0.016	0.990 ± 0.040	0.100 ± 0.020	0.990 ± 0.060
1.45	0.037 ± 0.007	1.000 ± 0.030	0.048 ± 0.010	1.000 ± 0.040	0.060 ± 0.020	1.000 ± 0.060
1.55	0.024 ± 0.006		0.025 ± 0.007		0.030 ± 0.010	
1.65	0.008 ± 0.002		0.010 ± 0.004		0.008 ± 0.003	
1.75	0.003 ± 0.001		0.001 ± 0.001		0.007 ± 0.003	
1.85	0.005 ± 0.003					
1.95	0.001 ± 0.001					

corrected $\rho(r; E_{\mathrm{T}})$ distribution in each $E_{\mathrm{T}}(\mathrm{jet})$ bin according to:

$$\Psi(r_n; E_{\mathrm{T}}) = \sum_{i=1}^{n} \rho(r_i; E_{\mathrm{T}}) \Delta r \,,$$

where i denotes the bin in a histogram.

Results of measurements of $\rho(r)$ and $\Psi(r)$ are presented in Tables 1–6.

Figure 2 shows the comparison of the differential jet shape $\rho(r)$ for carbon target for six bins of jet transverse energy (closed circles) and PYTHIA/FRITIOF predictions (open circles). The agreement between data and model predictions is quite good.

Figure 3 presents the ratios of the $\rho(r)$ measured with aluminium (closed circles) and tungsten (open circles) targets to carbon results. The results for aluminium and carbon targets are nearly the same (ratio is approximately

Table 5. Differential and integral jet shapes for tungsten 5 GeV $< E_T <$ 8 GeV

r	$E_T = 5$–6 GeV		$E_T = 6$–7 GeV		$E_T = 7$–8 GeV	
	ρ	Ψ	ρ	Ψ	ρ	Ψ
0.05	0.490 ± 0.050	0.049 ± 0.005	0.390 ± 0.040	0.039 ± 0.004	0.280 ± 0.040	0.028 ± 0.004
0.15	1.040 ± 0.060	0.154 ± 0.008	1.030 ± 0.070	0.142 ± 0.009	0.790 ± 0.070	0.107 ± 0.008
0.25	1.390 ± 0.060	0.290 ± 0.010	1.380 ± 0.080	0.280 ± 0.010	1.200 ± 0.100	0.230 ± 0.010
0.35	1.580 ± 0.060	0.450 ± 0.010	1.460 ± 0.070	0.430 ± 0.010	1.460 ± 0.090	0.374 ± 0.016
0.45	1.420 ± 0.050	0.590 ± 0.010	1.430 ± 0.060	0.569 ± 0.015	1.570 ± 0.090	0.530 ± 0.020
0.55	1.280 ± 0.040	0.720 ± 0.010	1.220 ± 0.050	0.691 ± 0.016	1.320 ± 0.070	0.660 ± 0.020
0.65	1.000 ± 0.040	0.820 ± 0.010	1.080 ± 0.040	0.800 ± 0.020	1.180 ± 0.060	0.780 ± 0.020
0.75	0.730 ± 0.030	0.894 ± 0.015	0.760 ± 0.030	0.880 ± 0.020	0.780 ± 0.040	0.860 ± 0.020
0.85	0.460 ± 0.020	0.940 ± 0.015	0.510 ± 0.020	0.930 ± 0.020	0.550 ± 0.030	0.910 ± 0.020
0.95	0.280 ± 0.010	0.968 ± 0.015	0.340 ± 0.020	0.960 ± 0.020	0.370 ± 0.020	0.950 ± 0.020
1.05	0.154 ± 0.008	0.983 ± 0.015	0.180 ± 0.010	0.980 ± 0.020	0.223 ± 0.016	0.970 ± 0.020
1.15	0.088 ± 0.005	0.992 ± 0.015	0.114 ± 0.008	0.990 ± 0.020	0.140 ± 0.010	0.990 ± 0.020
1.25	0.043 ± 0.003	0.996 ± 0.015	0.046 ± 0.004	1.000 ± 0.020	0.067 ± 0.007	0.990 ± 0.020
1.35	0.022 ± 0.002	0.998 ± 0.015	0.031 ± 0.003		0.037 ± 0.005	1.000 ± 0.020
1.45	0.009 ± 0.001	0.999 ± 0.015	0.014 ± 0.002		0.010 ± 0.002	
1.55	0.004 ± 0.001	1.000 ± 0.015	0.005 ± 0.001		0.008 ± 0.002	
1.65	0.002 ± 0.001		0.002 ± 0.001		0.002 ± 0.001	
1.75	0.001 ± 0.001		0.001 ± 0.001		0.002 ± 0.001	
1.85					0.001 ± 0.001	

Table 6. Differential and integral jet shapes for tungsten $E_T >$ 8 GeV

r	$E_T = 8$–9 GeV		$E_T = 9$–10 GeV		$E_T >$ 10 GeV	
	ρ	Ψ	ρ	Ψ	ρ	Ψ
0.05	0.180 ± 0.030	0.017 ± 0.003	0.120 ± 0.020	0.012 ± 0.002	0.210 ± 0.160	0.021 ± 0.016
0.15	0.640 ± 0.080	0.081 ± 0.008	0.560 ± 0.090	0.068 ± 0.009	0.540 ± 0.160	0.070 ± 0.020
0.25	1.200 ± 0.100	0.198 ± 0.015	1.500 ± 0.200	0.220 ± 0.030	1.700 ± 0.500	0.250 ± 0.050
0.35	1.650 ± 0.150	0.360 ± 0.020	1.400 ± 0.200	0.360 ± 0.030	1.500 ± 0.200	0.400 ± 0.060
0.45	1.610 ± 0.140	0.520 ± 0.030	1.330 ± 0.150	0.490 ± 0.040	1.300 ± 0.200	0.530 ± 0.060
0.55	1.260 ± 0.090	0.650 ± 0.030	1.400 ± 0.140	0.630 ± 0.040	1.200 ± 0.140	0.650 ± 0.060
0.65	1.120 ± 0.080	0.760 ± 0.030	1.020 ± 0.100	0.730 ± 0.040	0.900 ± 0.100	0.740 ± 0.060
0.75	0.740 ± 0.050	0.840 ± 0.030	0.930 ± 0.090	0.830 ± 0.040	0.800 ± 0.100	0.820 ± 0.060
0.85	0.620 ± 0.050	0.900 ± 0.030	0.640 ± 0.070	0.890 ± 0.040	0.460 ± 0.060	0.870 ± 0.060
0.95	0.420 ± 0.040	0.940 ± 0.030	0.440 ± 0.040	0.940 ± 0.040	0.430 ± 0.070	0.910 ± 0.060
1.05	0.280 ± 0.030	0.970 ± 0.030	0.240 ± 0.030	0.960 ± 0.040	0.300 ± 0.040	0.940 ± 0.060
1.15	0.152 ± 0.016	0.980 ± 0.030	0.160 ± 0.020	0.970 ± 0.040	0.280 ± 0.050	0.970 ± 0.060
1.25	0.080 ± 0.010	0.990 ± 0.030	0.140 ± 0.020	0.990 ± 0.040	0.130 ± 0.030	0.980 ± 0.060
1.35	0.045 ± 0.007	1.000 ± 0.030	0.060 ± 0.010	0.990 ± 0.040	0.100 ± 0.020	0.990 ± 0.060
1.45	0.032 ± 0.006		0.021 ± 0.005	1.000 ± 0.040	0.030 ± 0.010	0.990 ± 0.060
1.55	0.014 ± 0.003		0.024 ± 0.008		0.024 ± 0.009	1.000 ± 0.060
1.65	0.005 ± 0.002		0.007 ± 0.003		0.021 ± 0.009	
1.75	0.002 ± 0.001		0.004 ± 0.002		0.003 ± 0.002	

equal to unity). Statistically significant deviations from unity exist for the tungsten sample at $r \approx 0$ in E_T range 5 GeV $< E_T <$ 10 GeV and for large radius, $r > 1$ in the bin 5 GeV $< E_T <$ 6 GeV. Thus, on average, jets produced on tungsten nuclei have slightly different structure than jets for light nuclei. However the position of maximum energy flow is the same for all nuclear targets, $r_{\max} \approx 0.3$.

A jet is not a point-like object and has finite transverse size, its radius. In the cone algorithm, the jet radius is fixed and equal to the size of the cone chosen for jet selection, $R_{\mathrm{cone}} = 0.7 - 1.0$. In case of the k_T algorithm,

the jet radius is not fixed and extends to values $r > 1$. In the case of restricted acceptance over pseudo-rapidity (in the ϕ-direction the acceptance is not restricted) one can encounter problems with the selection efficiency of wide jets, when the jet radius exceeds the detector acceptance. We performed measurements for jets with axes within the pseudo-rapidities $\eta(\mathrm{jet}) = 3.5 \pm 0.1$. A realistic acceptance of HERA-B tracker (probability to register a track is greater than 10%) covers the pseudo-rapidity range $2.2 < \eta < 4.8$ (calorimeter has larger acceptance). Therefore, some fraction of selected jets must have par-
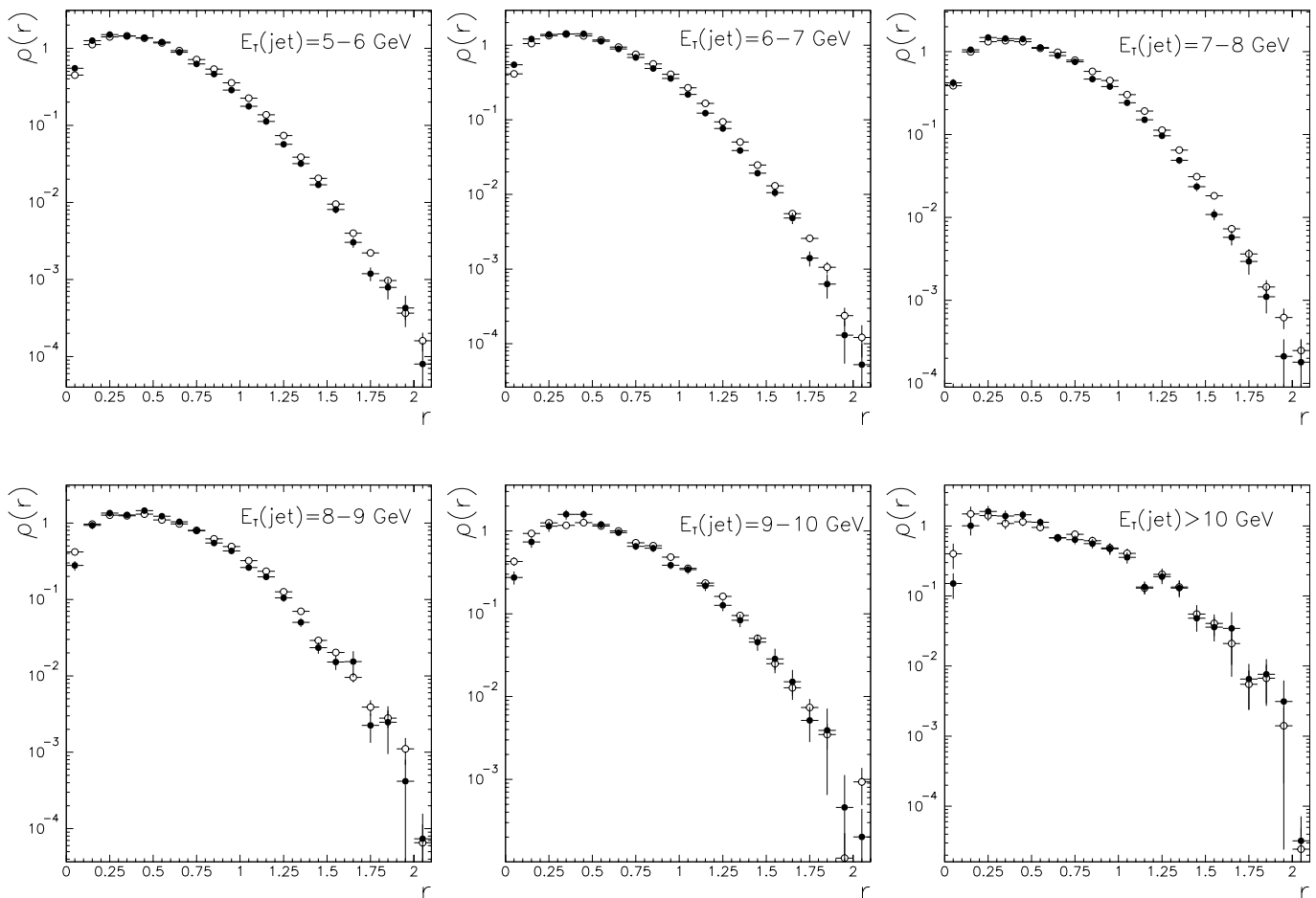
Fig. 2. Comparison of the differential jet shape $\rho(r)$ (*closed circles*) with PYTHIA/FRITIOF predictions (*open circles*) for the carbon target in every $E_T(\text{jet})$ bin

ticles outside the acceptance of our detector. However, the integral jet shape $\Psi(r)$ is about unity already for $r \approx 1$, i.e., almost all of the jet energy flow is concentrated within this cone and the whole jet is within the detector acceptance $(2.2 < \eta < 4.8)$.

Figure 4 demonstrates the correction factor $R(r; E_T)$ from (4) normalized to unity for the carbon target in the bin $E_T(\text{jet}) = 5.0$–6.0 GeV. The horizontal line is the mean value for this distribution. The variation of the correction factor does not exceed $\approx 25\%$ with respect to its mean value at radii $r \leq 1.5$ with good statistical errors. Thus we can expect that our systematic corrections are reliable within the effective interval of jet radii. Note here that correction factors for different nuclear targets agree well within their errors. Therefore they cancel out in the ratios of $\rho(r)$ for different nuclei, presented in Fig. 3.

7 Conclusion

We performed measurements of the differential $\rho(r)$ and integral $\Psi(r)$ jet shapes (3) in the range of jet transverse energies 5 GeV $< E_T(\text{jet}) <$ 14 GeV in proton–nucleus col-

lisions at a proton momentum 920 GeV/*c*. For jet selection, we used the longitudinally invariant k_T algorithm, defining jets according to standard Snowmass convention. We performed these measurements for three target nuclei – carbon, aluminium and tungsten. For systematic corrections to the differential jet shape we used bin-by-bin statistical corrections, based on a Monte Carlo simulation of jet production, in each bin of jet transverse energy. Integral jet shapes have been obtained by integration of the differential jet shapes.

We find good agreement between data and the predictions of the PYTHIA 6.2/FRITIOF 7.02 model with intrinsic transverse momentum of partons $k_T = 1$ GeV and independent fragmentation of partons according to the symmetric Lund scheme. The hadronization scheme in PYTHIA 6.2 at studied jet transverse energies does not include showering of the scattered parton. It instead produces the final state hadrons, mostly vector mesons, directly from the scattered parton. The agreement between our measurements and simulation shows that in the considered transverse energy range $E_T(\text{jet}) < 14$ GeV, the parton cascade is still not developed and the hadronization has mainly a non-perturbative nature, i.e., direct transition *parton* → *hadrons* and can be well reproduced by
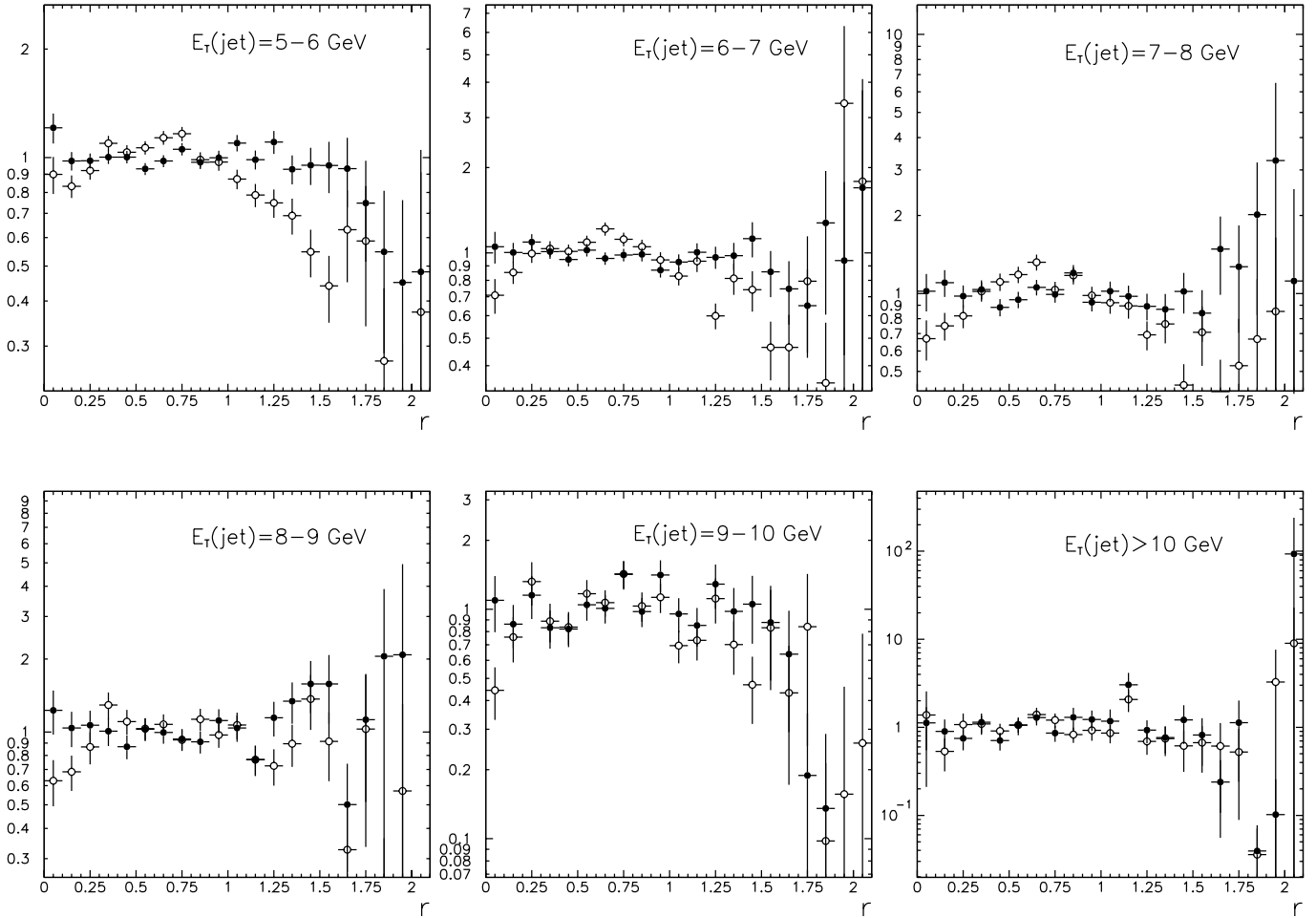
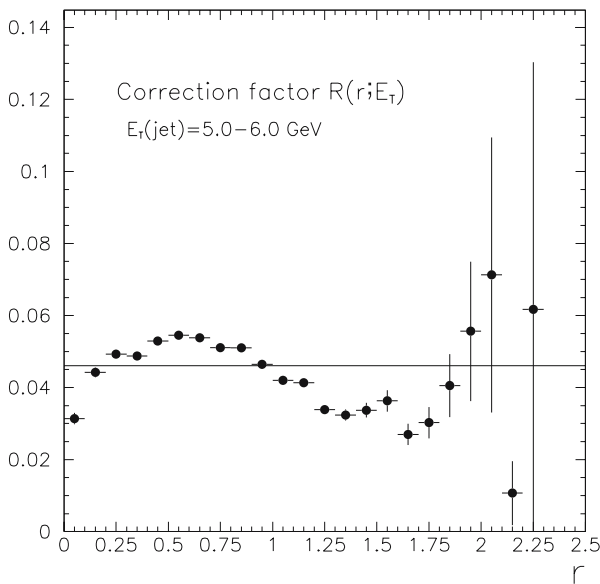**Fig. 3.** Ratios of the $\rho(r)$ measured with aluminium (*closed circles*) and tungsten (*open circles*) targets to carbon results in every $E_{\mathrm{T}}(\mathrm{jet})$ bin

Fig. 4. The dependence of the systematic correction factor $R(r; E_{\mathrm{T}})$ on the distance to the jet axis for carbon target in $E_{\mathrm{T}}(\mathrm{jet}) = 5.0$–$6.0$ GeV bin. The correction factor is normalized to unity

PYTHIA 6.2 with default parameters and independent fragmentation of outgoing partons.

From comparison of the differential jet shape $\rho(r)$ for different nuclei, we can conclude that the differences in jet properties for carbon and aluminium targets are small. Nevertheless, the transverse energy flow at small and large radii for the tungsten sample is slightly less than for light nuclei. Note here that this observation does not depend on our MC model due to cancellation of the systematic corrections in the ratios of $\rho(r)$ for different nuclei. This observation indicates some influence of the nuclear environment on the formation of jets in heavy nuclei, especially at lower transverse energies, $5\,\mathrm{GeV} < E_{\mathrm{T}}(\mathrm{jet}) < 6\,\mathrm{GeV}$. Possibly such a "broadening" of jets produced on a heavy nucleus occurs due to re-scattering of the jet hadrons on nucleons which effect must be small for light nuclei.

ulating discussions. We want also to thank all the HERA-B members who contributed in discussing and improving of the manuscript.

References

1. T. Akesson et al., Phys. Lett. B **128**, 354 (1983)
2. M. Banner et al., Phys. Lett. B **118**, 203 (1982)
3. G. Arnison et al., Phys. Lett. B **121**, 115 (1983)
4. CDF Collaboration, F. Abe et al., Phys. Rev. Lett. **62**, 613 (1989)
5. CDF Collaboration, F. Abe et al., Phys. Rev. Lett. **63**, 3020 (1989)
6. C. De Marzo et al., Nucl. Phys. B **211**, 375 (1983)
7. B.C. Brown et al., Phys. Rev. D **29**, 1895 (1984)
8. C. Stewart et al., Phys. Rev. D **42**, 1385 (1990)
9. G. Alverson et al., Phys. Rev. D **49**, 3106 (1994)
10. L.R. Cornell et al., Phys. Lett. B **150**, 322 (1985)
11. M.W. Arenton et al., Phys. Rev. D **31**, 984 (1985)
12. J.E. Huth et al., FERMILAB-Conf-90/249-E [E-741/CDF]
13. S.D. Ellis, D.E. Soper, Phys. Rev. D **48**, 3160 (1993)
14. S. Catani, Y.L. Dokshitzer, M.H. Seymour, B.R. Weber, Nucl. Phys. B **406**, 187 (1993)
15. S.D. Ellis, Z. Kunszt, D.E. Soper, Phys. Rev. Lett. **69**, 3614 (1992)
16. CDF Collaboration, F. Abe et al., Phys. Rev. D **45**, 1448 (1992)
17. S. Catani, Y.L. Dokshitzer, M.H. Seymour, arXiv:hep-ph/9707338
18. G. Marchesini, arXiv:hep-ph/0410275
19. HERA-B Collaboration, I. Abt et al., Eur. Phys. J. C **29**, 181 (2003) and references therein
20. K. Ehret et al., Nucl. Instrum. Methods A **446**, 190 (2000)
21. C. Bauer et al., Nucl. Instrum. Methods A **501**, 39 (2003)
22. W. Gradl et al., Nucl. Instrum. Methods A **461**, 80 (2001)
23. H. Albrecht et al., Nucl. Instrum. Methods A **541**, 610 (2005)
24. H. Albrecht et al., Nucl. Instrum. Methods A **555**, 310 (2005)
25. I. Ariño et al., Nucl. Instrum. Methods A **516**, 445 (2004)
26. G. Avoni et al., Nucl. Instrum. Methods A **461**, 332 (2001)
27. V. Eiges et al., Nucl. Instrum. Methods A **461**, 104 (2001)
28. T. Sjöstrand, P. Edén, C. Friberg, L. Lönnblad, G. Miu, S. Mrenna, E. Norrbin, Comput. Phys. Commun. **135**, 238 (2001) [LU TP 01-21, August 2001; arXiv: hep-ph/0108264]
29. H. Pi, An Event Generator for Interactions Between Hadrons and Nuclei – FRITIOF version 7.02. CERNLIB 97a
30. L. Apanasevich et al., hep-ex/9711017
31. L. Apanasevich et al., Phys. Rev. D **59**, 074 007 (1999)
32. S. Eidelman et al., Phys. Lett. B **592**, 1 (2004)